C. R. Physique 11 (2010) 245–256

Contents lists available at ScienceDirect

Comptes Rendus Physique

www.sciencedirect.com

Computational metallurgy and changes of scale / Métallurgie numérique et changements d'échelle

Phase field methods: Microstructures, mechanical properties and complexity

Méthodes de champs de phase : Microstructures, propriétés mécaniques et complexité

Alphonse Finel [a,*], Y. Le Bouar [a], A. Gaubert [b], U. Salman [a]

[a] *Laboratoire d'étude des microstructures, CNRS/ONERA, BP 72, 92322 Châtillon, France*
[b] *DMSM, ONERA, BP 72, 92322 Châtillon, France*

ARTICLE INFO

Article history:
Available online 30 August 2010

Keywords:
Phase field method
Polytwinned microstructure
Elasto-viscoplastic phase field model

Mots-clés :
Méthode des champs de phase
Microstructure lamellaire
Modèle champ de phase
élasto-visco-plastique

ABSTRACT

Structural and functional materials inherit their macroscopic properties from the complex microstructures they develop at mesoscale. We discuss here the ability of the phase field method to capture the physical mechanisms at the origin of these complex morphologies in two different situations. First, we analyze the polytwinned microstructures observed in martensitic alloys, and show that, due to the large rotations involved in the accommodation mechanism, a correct modeling of the microstructures requires the use of a geometrically nonlinear model. Second, we present an elasto-viscoplastic phase field model and show its application to the understanding of the rafting phenomena observed in superalloys under creep.

RÉSUMÉ

Les matériaux à vocation structurale et fonctionnelle doivent leurs propriétés macroscopiques aux arrangements microstructuraux complexes qu'ils développent à l'échelle mésoscopique. Nous discutons ici des potentialités de la méthode des champs de phase à reproduire correctement les mécanismes physiques responsables de la formation de ces microstructures dans deux situations différentes. Premièrement, nous analysons les microstructures lamellaires observées dans les alliages martensitiques, et nous montrons que, en raison des larges rotations de réseau requises par les mécanismes d'accomodation élastique, une modélisation correcte des microstructures nécessite l'utilisation d'une formulation géométriquement non-linéaire. Deuxièmement, nous présentons un modèle champ de phase élasto-visco-plastique et montrons son application à la compréhension des phénomènes de mises en radeau observés dans les superalliages en fluage.

1. Introduction

Macroscopic properties of metallic materials strongly depend on their microstructures, i.e. on the shape and spatial arrangement of the different phases that compose the materials. It is thus important to understand the role of the different driving forces that may influence microstructural evolutions, such as the relaxation of chemical free energies, the reduction

* Corresponding author.
E-mail address: Alphonse.Finel@onera.fr (A. Finel).

1631-0705/$ – see front matter
doi:10.1016/j.crhy.2010.07.014

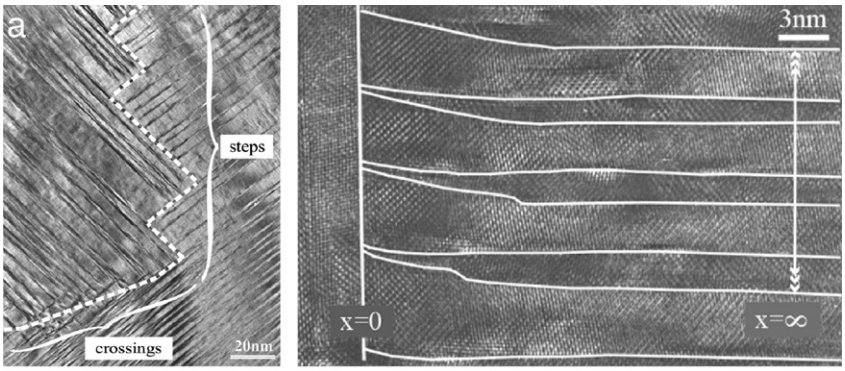

Fig. 1. (a) Typical TEM image of a macrotwin boundary in $Ni_{65}Al_{35}$. (b) Typical HRTEM image of nanoscale martensite needles close to one of the steps of the macrotwin image shown in (a). Taken from [2].

Fig. 1. (a) Image typique d'une macromacle dans $Ni_{65}Al_{35}$, observée en microscopie électronique en transmission. (b) Image typique d'aiguilles nanoscopiques de martensite au voisinage de la macromacle montrée en (a), observée en microscopie électronique à haute résolution. D'après [2].

of the elastic energies due to the internal stresses generated by the coherent accommodation of misfitting precipitates, the interplay with a plastic activity generated by an external loading or by migrating interfaces that separate phases with different underlying lattices, etc.

The phase field method has emerged as the most powerful method for tackling microstructure evolutions at mesoscale. The aim of this paper is to illustrate the use of this method in two different situations. First, we discuss the ability of the phase field method to reproduce the complex microstructures observed in martensitic alloys, where the most important mechanism is the coherent accommodation of the different martensitic variants along micro- and macro-twins. We show in particular that, due to the large material rotations required by the accommodation mechanism, a correct modeling is obtained only within the framework of nonlinear geometry. Second, we present an elasto-viscoplastic phase field model, based on the coupling to a continuous crystal plasticity model, and present its application to the study of ageing of a superalloy under creep loading.

2. Microstructures in martensites

2.1. Introduction

Martensitic phase transformations are displacive first order transitions that involve a shear dominated change of shape in the underlying crystal lattice from a high-symmetry phase, the austenite, to a degenerate low-symmetry phase, the martensite. Generally, the martensitic transition leads to very complex self-similar patterns that consist of twinned laminates on a wide range of length scales. An important mechanism at the origin of these complex morphologies is the lattice mismatch between the different variants of the low-symmetry martensite and the austenite. Specifically, lattice continuity at the interfaces between two variants and between any variant and the austenite enforces long-range elastic interactions. The resulting strain energy relaxes only through specific arrangements of twinned laminates that lead to a stress-free state characterized, at the scale of the laminates, by an invariant plane strain and, at a larger scale, by a very small average strain (see, for example, [1] for a general review).

We report here an investigation of the dynamics and morphology of macrotwins, such as those observed in $Ni_{65}Al_{35}$ [2–4], which undergoes a cubic-to-tetragonal martensitic transition upon cooling. These macrotwins are very common in martensites, as they are one of the building blocks of the elastic energy minimizing microstructures generally observed in the late stage of the transformation. Generally speaking, when the martensitic transition proceeds, multiply twinned martensitic plates are formed to accommodate the shape change and minimize the elastic energy. Each plate consists of two alternating and energetically equivalent martensitic variants, separated by so-called microtwin walls. When the transformation proceeds, each plate continues to grow: a macrotwin plane forms whenever two such polytwinned plates come into contact and try to accommodate. This interface often reveals a zig-zag configuration consisting in successive well defined steps, as seen in Fig. 1(a). Along one of these steps, the microtwins of one plate end at a twin wall of the other plate (see Fig. 1(b)), this wall thus providing the macrotwin interface. Important features of macrotwin interface are the specific shape adopted by the twins that are perpendicular to the boundary: as seen in Fig. 1(b), alternate twins narrow and bend when approaching the macrotwin interface.

The existence of these macrotwins requires rigid body rotations in order to maintain coherency along the microtwin walls and the macrotwin interface. These rotations are large because the shape change that characterizes the martensitic phase is often very large. Therefore, as shown below, the modeling of the formation of these macrotwins, and the reproduction of their specific morphologies, requires the use of a model that does not penalize rotations and hence is rotationally invariant.

A model is considered to be invariant under rotation if its energy and dissipation potential are unchanged when its deformation field is rotated (see, for example, [5,6] and the references therein). Most dynamic simulations of the martensitic transition have used strain-based models that are geometrically linear [7,8], i.e. that assume a linear relationship between the displacement and strain fields. This linearization simplifies greatly the formalism and allows the use of simple and stable numerical schemes. However, linear geometry is obtained as an approximation of the exact geometry under the assumption that displacements are infinitely small. As a consequence, the description is not invariant under rigid body rotations, in contrast to nonlinear geometry, which conserves the exact nonlinear relationship between the displacement and strain fields and is therefore invariant under rotation.

We present here a numerical comparison of geometrically nonlinear and linear models for identical physical problems from the thermodynamical, elastic and dissipative points of view and for the same physical parameters (mass density, elastic constants, damping coefficient and interfacial energy). We show that dynamic models for pattern formation in martensites with geometrically nonlinear strains capture physically relevant features not captured in geometrically linear models. In particular, we show that the experimentally observed macrotwin interfaces can only be reproduced within a nonlinear theory, as long-lived metastable states which cannot be reached in the geometrically linear model.

2.2. Viscoelastic model for martensitic phase transformations

A martensitic transformation is characterized by a displacement field $u(x) = y(x) - x$, where $y(x)$ and x are the coordinates of a material point in the deformed and undeformed states, respectively. Elastic energy F_L depends only on the deformation gradient $F = I + \nabla u$ and should be rotationally invariant. A simple way to enforce this property is to assume that F_L is only function of the Lagrangian tensor $\epsilon^{NL} = (F^T F - I)/2$, which amounts to assume, as usual, that elastic energy depends only on the length changes between material points. This functional dependence guaranties that F_L is invariant under rigid body rotation, simply because the strain tensor ϵ^{NL} itself is invariant if a rotation Q is applied to the deformed state:

$$\tilde{\epsilon}^{NL} = \frac{1}{2}\big((Q\,F)^T(Q\,F) - I\big) = \frac{1}{2}\big(F^T F - I\big) = \epsilon^{NL} \tag{1}$$

We use the superscript *NL* to stress the fact that the Lagrangian strain is a nonlinear function of the displacement gradient:

$$\epsilon^{NL}_{ij} = \frac{1}{2}\left(\frac{\partial u_i}{\partial x_j} + \frac{\partial u_j}{\partial x_i} + \frac{\partial u_k}{\partial x_i}\frac{\partial u_k}{\partial x_j}\right) \tag{2}$$

The geometrically linear approximation consists in neglecting the quadratic terms in the previous equation [1,6], leading to a linear strain tensor:

$$\epsilon^{L} = \frac{1}{2}\left(\frac{\partial u_i}{\partial x_j} + \frac{\partial u_j}{\partial x_i}\right) \tag{3}$$

i.e. $\epsilon^L = \frac{1}{2}(F + F^T) - I$. Obviously, ϵ^L is not rotationally invariant.

We consider here the square-to-rectangle transformation (we will comment on this choice below). The symmetry adapted linear combinations of strain components are:

$$e_1 = \epsilon_{11} + \epsilon_{22}, \qquad e_2 = \epsilon_{11} - \epsilon_{22}, \qquad e_3 = \epsilon_{12} = \epsilon_{21} \tag{4}$$

The quantity e_2 controls the square-to-rectangle transformation and is the primary order parameter. The first and third terms e_1 and e_3 play the role of secondary order parameters. To the lowest order, the corresponding local strain energy density is given by the following Landau potential:

$$F_L = a_2 e_2^2 + a_4 e_2^4 + a_6 e_2^6 + b_1 e_1^2 + b_3 e_3^2 \tag{5}$$

The coefficients a_2, a_4, a_6, b_1, and b_3 can be tuned to reproduce the elastic constants and the stress-free transformation strain of a specific alloy. We also include a gradient contribution, in the form of a Ginzburg term, in order to penalize interfaces between variants. This term of course breaks the scale invariance of the elastic medium and provides us with a length scale. For the sake of simplicity, we used here the following simple nonlocal density:

$$F_G = \frac{\beta}{2}(\Delta u_i)^2 \tag{6}$$

which fulfills the constraint of being rotationally invariant.

The dynamics of the martensitic transition is very often modeled through the use of a Time Dependant Ginzburg Landau theory which typically postulates that strain rates are proportional to a driving force derived from the thermodynamic potential. However, when the primary order parameter that controls the transition is an elastic long wavelength mode, as in martensitic transitions, this overdamped description is inadequate. Indeed, it is easy to show that, because of the conservation law of density, elastic long wavelength modes have always the time to propagate before to dissipate: these

modes are always underdamped. In other words, a correct description of the dynamics of the martensitic transition must incorporate inertial effects [9]. Therefore, we take into account a kinetic energy density $T = \frac{1}{2}\rho \dot{u}_i^2$. We also include the viscosity of the sound waves in the form of a Rayleigh dissipation density given by:

$$R = \frac{1}{2}\gamma_i \dot{e}_i^2 \tag{7}$$

where, for simplicity, the viscosity coefficients γ_i are supposed to be independent of the amplitudes of the local order parameters e_i. Finally, the dynamics of the system is given by the Langrange–Rayleigh equations:

$$\frac{\mathrm{d}}{\mathrm{d}t}\frac{\partial L}{\partial \dot{u}_i} - \frac{\partial L}{\partial u_i} = -\frac{\partial R}{\partial \dot{u}_i} \tag{8}$$

where $L = T - F_L - F_G$ is the Lagrangian density of the system. This dynamical equation may be written in the general form:

$$\rho \ddot{u}_i = \frac{\partial}{\partial x_j}\frac{\partial F_L}{\partial u_{i,j}} - \frac{\partial}{\partial x_j}\frac{\partial}{\partial x_k}\frac{\partial F_G}{\partial u_{i,jk}} + \frac{\partial}{\partial x_j}\frac{\partial R}{\partial \dot{u}_{i,j}} \tag{9}$$

where as usual $u_{i,j}$ and $u_{i,jk}$ stand for $\frac{\partial u_i}{\partial x_j}$ and $\frac{\partial^2 u_i}{\partial x_j \partial x_k}$, respectively.

This formulation fits both for geometrically nonlinear and linear models. These two models differ only in the way the strain components ϵ_{ij} enter, through the order parameters e_i, into the definitions of the local strain energy F_L and Rayleigh dissipation term R. In the following simulations, the dissipation term defined in Eq. (7) is treated linearly (i.e. with Eq. (3)) for numerical simplicity. The effects of a nonlinear dissipation term are discussed elsewhere [10,11]. However, we mention here that the models with linear and nonlinear dissipation terms lead to very similar final microstructures, simply because dissipation is vanishingly small in the late stages of the dynamics.

2.3. Numerical results

Our aim is to analyze macrotwins associated with the cubic-to-tetragonal transformation, but here we consider the simpler 2D square-to-rectangle transition. The latter may be interpreted as a 3D cubic-to-tetragonal transition with the following restrictions. Consider a 3D crystal where the displacement field fulfills the following constraints: components u_1 and u_2 are translationally invariant along axis x_3 and the third component u_3 varies linearly with x_3, i.e. $u_1(x_1, x_2, x_3) = u_1(x_1, x_2)$, $u_2(x_1, x_2, x_3) = u_2(x_1, x_2)$ and $u_3(x_1, x_2, x_3) = \lambda x_3$. The strain tensor ϵ_{ij} then adopts the following restricted form:

$$\begin{pmatrix} \epsilon_{11}(x,y) & \epsilon_{12}(x,y) & 0 \\ \epsilon_{21}(x,y) & \epsilon_{22}(x,y) & 0 \\ 0 & 0 & \lambda + \frac{\lambda^2}{2} \end{pmatrix} \tag{10}$$

where we used the nonlinear formulation. Now, let variants I and II be the martensitic variants with tetragonal axis parallel to axes x_1 and x_2, respectively, and let $U = F - I$ be the transformation strain that transforms the austenite into variant I:

$$U = Diag[\beta, \alpha, \alpha] \tag{11}$$

Obviously, if $\lambda = \alpha - 1$, any laminate composed of tetragonal variants I and II, and hence with {110}-type twin walls, will be stress-free. Therefore, from the microstructural and energetic point of views, this laminate is exactly equivalent to a 2D laminate consisting in the two rectangular variants of the square-to-rectangle transition with {11}-type twin walls. In other words, we conclude that our 2D model should reproduce correctly the morphology of 3D multiple laminate structures formed by tetragonal variants I and II and the corresponding macrotwins, such as those observed in the late stage of the martensitic transition. Of course, we cannot expect that a 2D modeling will capture correctly the dynamics itself, in particular when austenite and martensite coexist. However, the results reported below concern specifically the stability of macrotwins in the late stage of the transition.

The evolution equations were solved using methods described in Refs. [10,12]. Equations are first written in a dimensionless form using adapted units for mass density ($\rho_0 = 6.657$ g/cm^3), time ($t_0 = 10^{-13}$ s), spatial coordinate ($d_0 = 0.1$ nm) and energy density ($f_0 = 29.8$ GPa). The dimensionless parameters used here are the following: $\tilde{\rho} = 1$, $\tilde{a}_2 = -0.40$, $\tilde{a}_4 = -2.18$, $\tilde{a}_6 = 119$, $\tilde{b}_1 = 2$, $\tilde{b}_3 = 2$, $\tilde{\gamma} = 0.1$, $\tilde{\beta} = 0.1$, where $\tilde{\alpha}$ refers to the dimensionless counterpart of the physical quantity α. These parameters have been chosen to make our 2D system representative of the situation in $Ni_{65}Al_{35}$ [13]. The simulations are carried out on a grid of size 1024×1024 that corresponds to a physical size of 0.1 μm × 0.1 μm. The interfaces within the simulations correspond to an interface width of the order of 0.3 nm, which is close to typical interface widths observed in the experiments.

In order to analyze the stability of macrotwins such as those observed in Fig. 1, the simulations start with the initial configuration shown in Fig. 2(a). It consists in four macrotwins between laminates formed by alternating sequences of variants I and II. The deviatoric order parameter field e_2 is initialized to small values, proportional to the equilibrium value of the corresponding variant. The initial velocity of the displacement fields u_i is also set to zero.

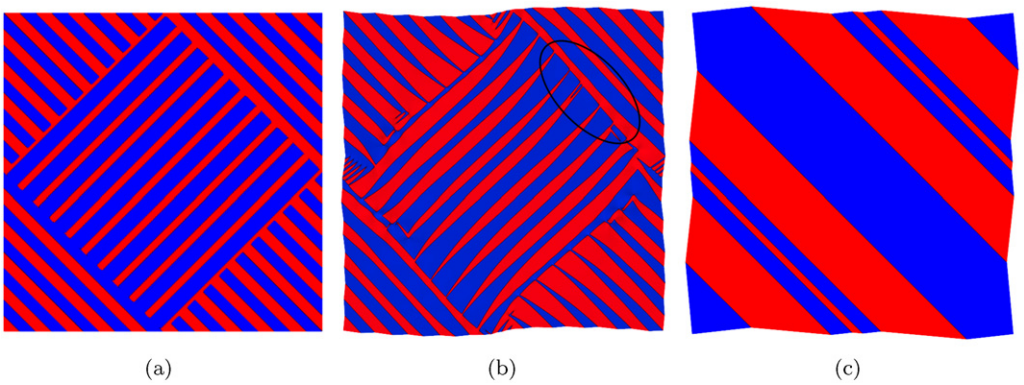

Fig. 2. (a) Initial microstructure. (b) Final microstructure obtained in the geometrically nonlinear model. (c) Final microstructure in the geometrically linear model.

Fig. 2. (a) Microstructure initiale. (b) Microstructure finale obtenue avec le modèle géométriquement non-linéaire. (c) Microstructure finale obtenue avec le modèle géométriquement linéaire.

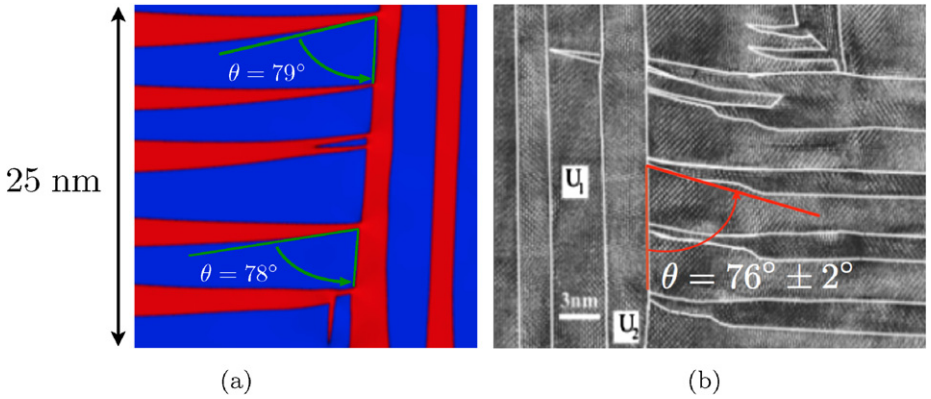

Fig. 3. Comparison between simulated microstructure and experiments. (a) Enlargement of circled region in Fig. 2(b), rotated by 45°. (b) HRTEM image of a macrotwin boundary [4].

Fig. 3. Comparaison entre microstructure simulée et observation expérimentale. (a) Agrandissement de la région cerclée de la Fig. 2b, après rotation de 45°. (b) Image haute résolution d'une macromacle dans $Ni_{65}Al_{35}$ [4].

The dynamics is first ran within the exact nonlinear geometry scheme. The corresponding long-lived microstructure is shown in Fig. 2(b). We observe that the microtwins in the neighborhood of macrotwin boundaries display new features. In particular, a variant that meets a perpendicular lamella made of the same orientational variant is seen to bend and to narrow when approaching the macrotwin interface. Finally, the final state obtained using the nonlinear modeling still displays the initial macrotwin boundaries, but characterized now, on one side, by alternating sequences of variants that narrow and bend when approaching the macrotwin boundary. We mention that this final state, although metastable, does not evolve anymore. For comparison, we present in Fig. 2(c) the microstructural evolution within the linear geometry. We used the same material parameters as for the nonlinear modeling. The only difference is that we used here Eq. (3) instead of Eq. (2). We note that the final microstructure is completely different from the one obtained with the geometrically nonlinear model. We will comment further on that point below.

In Fig. 3, enlargement of the circled region in Fig. 2(b) is shown together with a transmission microscope image of a macrotwin boundary in NiAl [4] for a convincing comparison between the nonlinear model and the experimental observation. We indeed observe that the tapering and bending of alternating variants is well reproduced by the nonlinear model. We note also that needle splitting and hook-type forms are also reproduced.

2.4. Discussion

The driving force for the development of these microstructures is, of course, the reduction of the strain energy. The underlying mechanism is the following. Consider a macrotwin interface parallel to a (110) plane, as the one sketched in Fig. 4(a). This situation corresponds to the macrotwin boundary in the upper right corner of the final configuration displayed in Fig. 2(b). Accommodation, along the (110) twin plane, of variant I (on the right side of the plane) and of

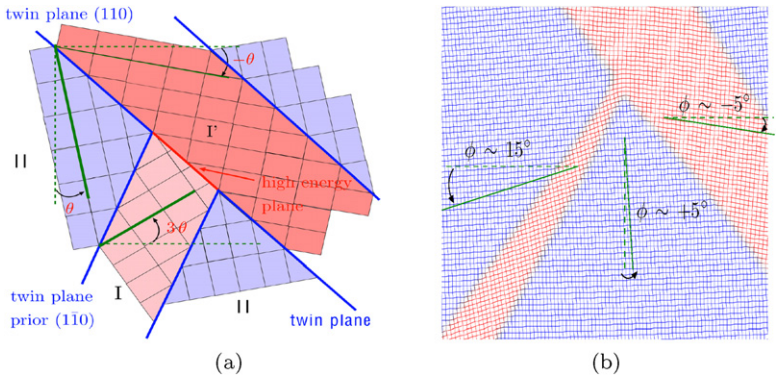

Fig. 4. (a) Schematic representation of a macrotwin boundary between two differently oriented laminates, (b) simulated microstructure at the grid scale in the nonlinear model. The angle ϕ measures the rotations of variants with respect to the reference state.

Fig. 4. (a) Représentation schématique d'une macromacle entre deux domaines lamellaires différents. (b) Représentation de la microstructure simulée à l'échelle de la grille de discrétisation. L'angle ϕ mesure les rotations de variants par rapport à l'état de référence.

variant II (on the left side) requires rotations equal to $-\theta$ and $+\theta$, respectively.[1] Now, as variant II has already been rotated by $+\theta$, accommodation along the former $(1\bar{1}0)$ twin plane that collides with the macrotwin boundary requires that variant I rotates by 3θ in order to fit coherently with variant II. As a result, the former $(1\bar{1}0)$ twin wall must rotate by 2θ. This is at the origin of the bending of the twin walls that we observe in the simulation as well as in the experiment. We note also that the different rotations displayed by the variants as well as the amplitude of the bending observed in the simulation are numerically close to the expected values (see Figs. 3 and 4(b)). Another important feature of the previous accommodation mechanism is that it leads, along the macrotwin boundary, to interfaces between domains made of the same orientational variant (i.e. domains with identical deviatoric strain e_2) but with very different rotations. Specifically, in the situation depicted in Fig. 4(a), there is an interface between two domains of variant I that have been rotated by $-\theta$ and 3θ, respectively, leading to a high strain energy density along this interface. The system will try to shorten this high energy interface and, consequently, to lengthen the neighboring low energy twin walls. This mechanism is at the origin of tapering of alternate variants observed in the simulation and in the experiment shown in Fig. 3.

In brief, the bending and narrowing of alternate variants along a macrotwin boundary requires large local rigid body rotations (as high as 3θ, with $\theta \sim 5°$ for the parameters that we used to calibrate our potential). This illustrates the importance of using a rotationally invariant model.

Indeed, as shown in Fig. 2(c), where we report the final microstructure obtained within the linear modeling, the time evolution with the linear model is completely different. As in the nonlinear modeling, stress accommodation operates first at short length scales (not shown) and we observe the formation of needles in the neighborhood of the macrotwin boundaries. However, in further time steps, the needles retract and martensite laminates start to disappear in favor of large martensitic domains. Finally, the geometrically linear model produces a final state that extends across the whole domain, i.e., a simple laminate, shown in Fig. 2(c).

The differences between the microstructures obtained within the two models can be directly linked to the role of rotations involved by the accommodation mechanism. For a quantitative understanding of this point, we present in Fig. 5 the variation of the strain energy density of an homogeneous variant as function of the angle ϕ of an applied rigid body rotation, according to the linear model, i.e. using Eqs. (4) and (5) with the linear relation of Eq. (3) (we recall that this strain energy density does not depend on ϕ if a nonlinear scheme is used). As seen in Fig. 5, the strain energy density difference between the martensite and the austenite, varies very slowly with ϕ for small angles, say up to approximately 10°. However, most of the stabilization of the martensite is lost for higher rotations. Indeed, rotations of the order of 3θ, as those involved in the stabilization of the needles within the nonlinear model, almost exhaust the energy difference between martensite and austenite. This unphysical behavior is the reason why the dynamics within the linear model cannot sustain the bending and tapering of the microtwins and, therefore, cannot stabilize the macrotwin boundaries observed in the nonlinear model and in the experiment discussed above.

2.5. Conclusion

In the first part of this article, we have presented a numerical comparison between two dynamical models for understanding the formation of complex microstructures observed in materials undergoing a martensitic phase transformation. The first model incorporates a geometrically nonlinear strain tensor, to insure that the strain energy is rotationally invariant, whereas the second one is based on its geometrically linear approximation. The linear model is commonly used

[1] The angle θ is given by $\tan\theta = \frac{|\alpha-\beta|}{\alpha+\beta}$, where α and β are the entries of the transformation strain U defined in Eq. (11).

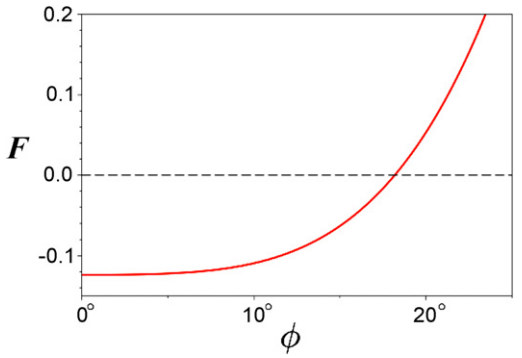

Fig. 5. Strain energy density of a homogeneous variant as a function of the angle ϕ of a rigid body rotation in the linear model.

Fig. 5. Densité d'énergie élastique d'un variant martensitique homogène en fonction de l'angle de rotation rigide ϕ, dans la formulation géométriquement linéaire.

as an approximate approach for studying the dynamics of martensitic phase transformations. Our findings show that this approximation cannot capture and reproduce the physical mechanisms at the root of the stabilization of the late stage microstructures observed in martensites. In particular, we show that the model with geometrically nonlinear strains produces final metastable states with multiple laminates, separated by stable macrotwin interfaces along which bending, tapering and splitting of microtwin needles are observed, in agreement with experiment. On the other hand, the linear model produces final states that are always simple laminates. We argue that the absence of stable macrotwin boundaries in the linear model is due to the penalty resulting from material rotations required for the coherent accommodation of the deviatoric strain along macrotwins.

3. Rafting in Ni-base superalloys

3.1. Introduction

Ni-base superalloys are employed to manufacture gas turbine blades because of their excellent mechanical behavior at high temperature (up to 1100 °C) and under loading. This behavior is mainly the result of the hardening induced by coherently precipitated cubes of γ' phase surrounded by thin channels of γ disordered matrix. Under creep loading at high temperature, the so-called rafting phenomenon is observed. γ' precipitates coarsen in an anisotropic way to form platelets. From a metallurgical point of view, rafting has been the subject of a great number of studies. It has been reported that raft orientation is controlled by different parameters such as the sign of the lattice mismatch, the sign of the external loading and the differences in elastic constants between matrix and precipitates. In the mean time, several authors underline that plastic activity plays an important role in this morphological evolution [14–17]. A great number of models has been developed in order to predict raft orientation, first within a simple elastic frame [18,19] and more recently adding the plastic strain influence [20].

However, an accurate description of the rafting kinetics and of the raft shape can only be reached if the complexity of the microstructure evolution is taken into account. Phase field models (PFM) are now recognized as the reference approach to study microstructural evolutions at mesoscale, especially when topological changes occur and elastic strains are present. Several phase field studies have obtained coarsened morphologies under applied load along a cubic axis (e.g. [19]) and the predicted anisotropy of the rafted microstructure is consistent with the experimental observations. However, these approaches neglect the important plastic activity which is coupled to the microstructural evolution. What we propose here is to improve PFM introducing the role of plastic strains on the microstructure evolution.

The introduction of plastic strains in PFM has already been treated by modeling dislocations dynamics [21–23]. Dislocations are represented by their plastic eigenstrains and act individually through the elastic field they generate. Large scale simulations taking into account the mutual interactions between all the glide systems and the evolving γ/γ' microstructure are computationally very intensive. In addition, in these models, the dislocation dynamics is only based on glide, and activated processes such as cross-slip and climb are not taken into account. These thermally activated processes are important when considering high-temperature evolutions as it is the case under creep conditions. In this work, we have chosen to couple the phase field model with a plasticity model directly written at the continuum level. The plastic activity is therefore described by a plastic strain tensor field, whose temporal evolution follows a viscoplastic constitutive law. In this approach, the consequences of cross-slip and climb are at least partially included through the adjustment of the viscosity coefficients.

Up to now, only few attempts have been made to couple phase field models with continuous plastic models. Ubachs et al. [24] have already applied such a law to compute the stress field in a phase field simulation, but without coupling diffusion and mechanical effects. More recently, Refs. [25,26] have coupled Continuum Mechanics to PFM to study grain growth and hydride precipitation in zirconium, and Ref. [27] has proposed a general constitutive framework to incorporate mechanical

behavior laws into phase field models. Finally, in a previous work, we have developed a phase field model coupled to an *isotropic* continuous plasticity model to study rafting in a model superalloy [28].

3.2. Phase field model

PFM consists in describing a microstructure by the means of continuous fields. A γ/γ' structure is characterized by the concentration field $c(\vec{r},t)$ and three order parameters fields $\eta_i(\vec{r},t)$. These fields are the local amplitude of the three [100] ordering waves that are needed at mesoscale to represent any inhomogeneous distribution of the four translation variants of the γ' phase. The temporal evolution of the microstructure can be obtained by solving the Cahn–Hilliard equation in the case of the concentration field, and Allen–Cahn equations for non-conserved fields, respectively:

$$\frac{\partial c}{\partial t} = M\nabla^2 \frac{\delta F}{\delta c} \tag{12}$$

$$\frac{\partial \eta_i}{\partial t} = -L\frac{\delta F}{\delta \eta_i} \tag{13}$$

where the kinetic coefficient L and the mobility coefficient M are assumed constant. $F = F_{GL} + F_{el} + F_{vp}$ is the total free energy of the system. The following paragraphs describe the evaluation of the each component of the free energy, respectively the Ginzburg–Landau, the elastic and the viscoplastic energies.

The non-equilibrium "chemical" free energy of the stress-free crystal may be approximated by a standard Ginzburg–Landau functional:

$$F_{GL} = \int_V \left[f_{homo}\big(c,\{\eta_i\}\big) + \frac{\lambda}{2}|\nabla c|^2 + \frac{\beta}{2}\sum_{i=1}^{3}|\nabla\eta_i|^2 \right] \mathrm{d}V \tag{14}$$

where the gradient coefficients λ and β are assumed constant. In the above expression, we have used isotropic gradient terms, which imply isotropic interfacial energies. As usual, the free energy density $f_{homo}(c,\{\eta_i\})$ of a homogeneous system characterized by the concentration c and the order parameters η_i is estimated using a polynomial expansion with respect to the order parameters. Following [29], we stop the polynomial expansion to the lowest possible order and we assume a very simple concentration dependence for the coefficients of the expansion:

$$f_{homo}\big(c,\{\eta_i\}\big) = \Delta f\left[\frac{1}{2}(c-c_\gamma)^2 + \frac{\mathcal{B}}{6}(c_2-c)\sum_{i=1,3}\eta_i^2 - \frac{\mathcal{C}}{3}\eta_1\eta_2\eta_3 + \frac{\mathcal{D}}{12}\sum_{i=1,3}\eta_i^4\right] \tag{15}$$

where Δf is the energy density scale of the model and c_2 is an arbitrary concentration chosen between the equilibrium concentrations c_γ and $c_{\gamma'}$ of the coexisting phases.

The elastic energy of a coherent microstructure of volume V reads:

$$F_{el} = -V\,\underset{\sim}{\sigma}^a : \bar{\underset{\sim}{\varepsilon}} + \frac{1}{2}\int_V \underset{\sim}{\sigma} : \underset{\sim}{\varepsilon}^{el}\,\mathrm{d}V \tag{16}$$

where $\underset{\sim}{\sigma}^a$ is the applied stress tensor, $\underset{\sim}{\sigma}$ is the stress tensor, $\bar{\underset{\sim}{\varepsilon}}$ is the average strain tensor and $\underset{\sim}{\varepsilon}^{el}$ is the elastic strain tensor. This tensor is related to the total strain tensor $\underset{\sim}{\varepsilon}$, the transformation strain $\underset{\sim}{\varepsilon}^0$ and the plastic strain $\underset{\sim}{\varepsilon}^p$ through

$$\underset{\sim}{\varepsilon}(\underline{\mathbf{r}}) = \underset{\sim}{\varepsilon}^{el}(\underline{\mathbf{r}}) + \underset{\sim}{\varepsilon}^{0}(\underline{\mathbf{r}}) + \underset{\sim}{\varepsilon}^{p}(\underline{\mathbf{r}}) \tag{17}$$

Assuming Vegard's law, the stress-free strain tensor is purely dilatational and its diagonal components ε^0 can be expressed using the concentration field:

$$\varepsilon^0(\underline{\mathbf{r}}) = \frac{\delta}{c_{\gamma'}-c_\gamma}\big(c(\underline{\mathbf{r}}) - \bar{c}\big) \tag{18}$$

where $\bar{c}$ is the average concentration and δ is the misfit.

Plastic deformation of superalloys mainly results from the movement of dislocations inside the γ phase. An important point is that the easy movement of dislocations (glide) is only possible within a given set of crystallographic planes (slip planes), and this results in a very anisotropic plastic response. Dislocations are usually divided into slip systems: dislocations belonging to the same slip system s share a common orientation of their glide plane and their glide implies a slip along the same direction $\underline{\mathbf{l}}^s$. The glide of dislocations belonging to a given slip system s induces at the continuous level a plastic strain proportional to the orientation tensor $\underset{\sim}{\mathbf{m}}^s$ defined as

$$\underset{\sim}{\mathbf{m}}^s = \frac{1}{2}\big(\underline{\mathbf{l}}^s \otimes \underline{\mathbf{n}}^s + \underline{\mathbf{n}}^s \otimes \underline{\mathbf{l}}^s\big)$$

where $\underline{\mathbf{n}}^s$ is the normal to the slip plane. At the continuous level, an effective way of accounting for the anisotropy of the plastic activity is to use the crystal plasticity model proposed by Cailletaud et al. [30,31]. In this model, the geometry of the slip systems is used to write, in a small perturbation framework, the total plastic deformation as the sum of the shear strain γ^s over all slip systems s.

$$\underset{\sim}{\varepsilon}^p = \sum_s \gamma^s \underset{\sim}{\mathbf{m}}^s \tag{19}$$

The plastic shear γ^s on each slip system is determined from a constitutive model. This model has to include two important characteristics of plasticity. First, the movement of dislocations, and therefore the plastic activity, is only possible when the applied stress reaches a critical value. More precisely, according to Schmidt criterion, the slip system s is only active when the resolved shear stress

$$\tau^s = \underset{\sim}{\sigma} : \underset{\sim}{\mathbf{m}}^s \tag{20}$$

reaches a critical value. The second important property is that, during plastic deformation, a crystal becomes harder and harder to deform plastically (strain hardening). One of the most simple models that incorporate these properties is the Norton's type flow rule:

$$\dot{\gamma^s} = \left\langle \frac{|\tau^s - x^s| - {r_0}^s}{k} \right\rangle^n sign\left(\tau^s - x^s\right) \tag{21}$$

In Eq. (21), $\langle a \rangle$ is the positive part of a, and n and k are the Norton's law coefficients. In the initial configuration, the hardening variable x^s is set to zero, implying that r_0^s corresponds to the initial threshold for plastic activity. During plastic deformation, the hardening variable x^s evolves in order to account for kinematic hardening. Its temporal evolution is given by the following nonlinear behavior:

$$x^s = c^s \alpha^s \quad \text{with } \dot{\alpha}^s = \dot{\gamma^s} - d^s |\dot{\gamma^s}| \alpha^s \tag{22}$$

In Eq. (22), α^s denotes the kinematic hardening state variable, c_s and d^s are phenomenological coefficients. This choice is consistent with the following viscoplastic free energy:

$$F_{vp} = \frac{1}{2} \sum_s c_s (\alpha_s)^2 \tag{23}$$

Therefore, in the present phase field model, the plastic activity is described through the temporal evolution of several new fields: γ^s, $\underset{\sim}{\varepsilon}^p$ and α_s (or x^s).

The procedure used for the numerical integration of the new model is the following. At each time step, we first solve for the mechanical equilibrium, assuming that the stress-free strain $\underset{\sim}{\varepsilon}^0(\underline{\mathbf{r}})$ and the plastic strain $\underset{\sim}{\varepsilon}^p(\underline{\mathbf{r}})$ are fixed quantities. This is realized using a fixed point algorithm. At the end of the mechanical equilibrium step, we end up with the updated value of the total strain tensor $\underset{\sim}{\varepsilon}(\underline{\mathbf{r}})$ and of the stress tensor $\underset{\sim}{\sigma}(\underline{\mathbf{r}})$. The second step of the procedure is to solve the viscoplastic kinetic equations. To do so, we compute the resolved shear stress on each slip system $\tau^s(\underline{\mathbf{r}})$ using (20). Then the new values of the plastic fields γ^s and $\alpha_s(\underline{\mathbf{r}})$ are computed, with an Euler scheme, using the kinetic Eqs. (21) and (22). The new value of the plastic strain $\underset{\sim}{\varepsilon}^p$ is obtained using (19). Finally, the last step of the procedure is to compute the evolution of the concentration field $c(\underline{\mathbf{q}})$ and of the order parameter fields $\eta_i(\underline{\mathbf{q}})$, with a semi-implicit scheme, using the usual kinetic Eqs. (12) and (13) in Fourier space.

3.3. Numerical inputs

The method used to select relevant model's parameters at 950 °C is detailed in [32], and the numerical values are gathered in Table 1. In the viscoplastic model, we have neglected the plastic activity in the γ' precipitates and we have used the results of monotonic and cyclic experiments in order to select viscoplastic coefficients representative of the plastic behavior of the γ matrix inside channels whose width is 150 nm.

3.4. Results

The microstructure evolution during a creep loading of 300 MPa at 950 °C is presented in Fig. 6. The initial condition is a cuboidal microstructure obtained in a separate simulation from a disordered state in stress-free condition. In order to estimate the relative importance of plastic and elastic driving forces during rafting, we have first artificially turned off the viscoplastic activity in the model (top row in Fig. 6). The bottom row are the results of the elasto-viscoplastic phase field model.

Table 1
Parameters of the model at 950 °C. Elastic constants are given in GPa and the diffusion coefficient $D = M\Delta f$ in $m^2\,s^{-1}$. The viscoplastic coefficients of the γ phase refer to the octahedral slip systems. c_s and r_0^s are expressed in MPa and k in MPa $s^{1/n}$.

Tableau 1
Paramètres du model pour $T = 950$ °C. Les constantes élastiques sont en GPa et les coefficients de diffusion $D = M\Delta f$ en $m^2\,s^{-1}$. Les coefficients de viscoplasticité de la phase γ réfèrent aux systèmes de glissement octaédriques. c_s et r_0^s sont exprimés en MPa et k en MPa $s^{1/n}$.

c_γ	c'_γ	C_{11}^γ	C_{12}^γ	C_{44}^γ	$C_{11}^{\gamma'}$	$C_{12}^{\gamma'}$	$C_{44}^{\gamma'}$	δ	D	n	k	r_0^s	c_s	d_s
0.15	0.23	197	144	90	193	131	97	−0.1 %	4.10^{-16}	5	750	12	7.10^4	2500

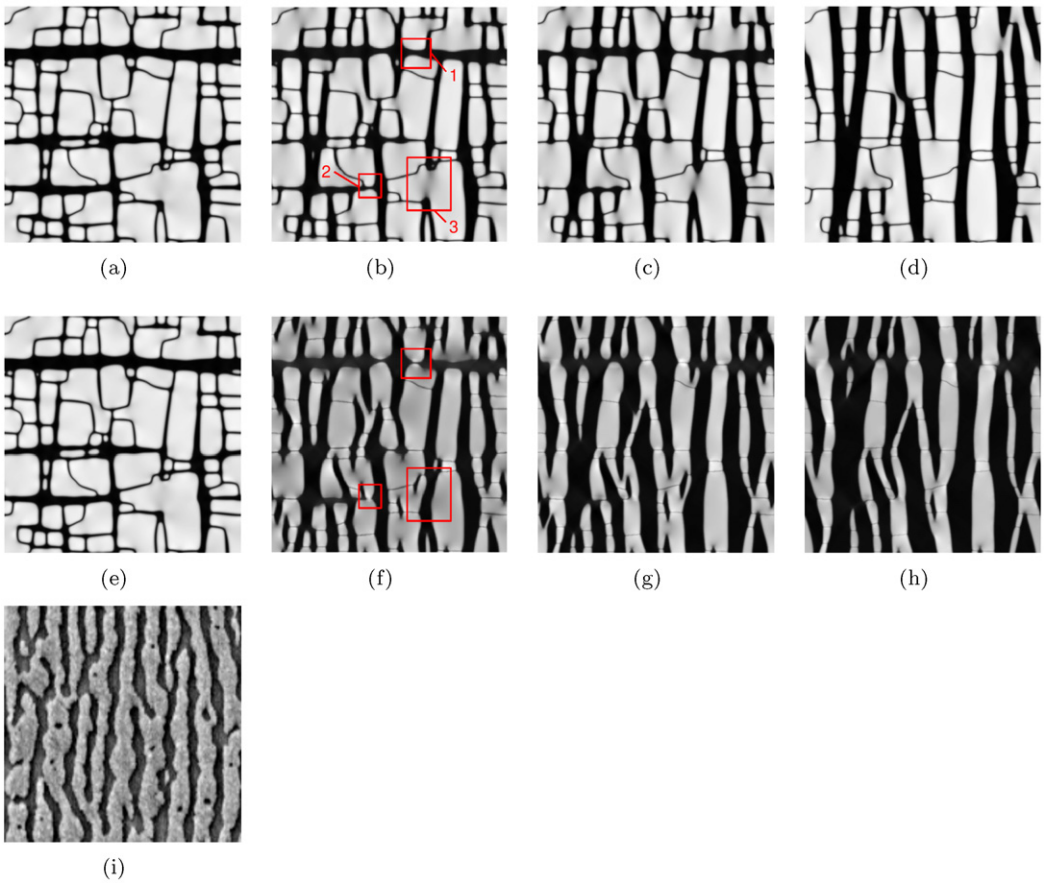

Fig. 6. Simulated microstructure evolution obtained during a creep loading of 300 MPa at 950 °C, the tensile axis being horizontal. Top row: predictions of the elastic phase field model at (a) $t = 0$, (b) $t = 5$ h, (c) $t = 10$ h and (d) $t = 40$ h. Bottom row, (e) to (h): simulation with the elasto-viscoplastic model at the same times. The simulations are performed using a 512×512 uniform grid. Bottom row (i): typical experimental rafted microstructure (creep test at 950 °C and 300 MPa) taken from [33].

Fig. 6. Simulation de l'évolution d'une microstructure sous chargement en fluage de 300 MPa à 950 °C, l'axe de tension étant horizontal. Rangée du haut : prédiction obtenue avec le modèle de champ de phase élastique pour (a) $t = 0$, (b) $t = 5$ h, (c) $t = 10$ h et (d) $t = 40$ h. Rangée du bas, (e) à (h) : simulation avec le modèle élasto-visco-plastique, pour les mêmes instants. Les calculs sont effectués sur une grille uniforme de taille 512×512. Rangée du bas (i) : microstructure en radeau typique (test de fluage à 950 °C et 300 MPa), d'après [33].

It is clear that rafting of precipitates is observed in the two simulations presented in Fig. 6. The raft orientation is perpendicular to the tensile axis, in agreement with experimental observations (e.g. [33]). However, the comparison of the predictions of the elastic and elasto-viscoplastic models reveals that plastic activity influences both the microstructure evolution and its kinetics.

First, plastic activity changes the global shape of the rafts. Indeed, whereas elastic rafts are quite straight and well-aligned along cubic directions, they are more irregular and with a wavy shape in the elasto-viscoplastic simulation. As it can be seen in Fig. 6(i), the wavy shape of the raft is consistent with observations of rafted microstructures in AM1 superalloys. Close to the raft misorientations, the plastic strain component $\varepsilon_{11}^p(\underline{\mathbf{r}})$ shows strong maxima along the directions at 45° from the tensile loading axis, i.e. along directions where the Schmid factor is maximum. It means that the wavy shape of the rafts is the result of the anisotropy of the plastic activity.

Another obvious consequence of the plastic activity is the speed-up of the morphological changes leading to the rafted structure. This point is illustrated after 5 h of creep by the three characteristic areas presented in Figs. 6 (b) and (f). Area labeled 1 shows that two γ' domains, which are in antiphase relationship and which come close to each other to form a raft, are still quite far away from each other in the elastic simulation after 5 h, whereas they are already in contact in the elasto-viscoplastic simulation. In the area labeled 2, two γ' domains of the same variant coalesce to form a raft. After 5 hours, the domains are still well separated in the elastic simulation, while they have already coalesced in the elasto-viscoplastic simulation. Finally, rafting proceeds not only by directional coalescence of precipitates, but also by splitting of large precipitates leading to the creation of vertical channel of γ structure. This microstructural evolution can be seen inside the area labeled 3. Comparison of Figs. 6 (b) and (f) reveals that the splitting of precipitates is also much faster when plastic activity is introduced in the model. As a conclusion, our simulations predict that plastic activity significantly increases the rafting kinetics.

From Fig. 6, it is also clear the precipitate phase fraction evolves during the microstructural evolution, especially when plastic activity is taken into account. The phase fraction changes originate from the modification of the γ and γ' concentrations between the initial coherent microstructure and the rafted microstructure where coherency stresses are partially relaxed by plasticity. However, from a quantitative point of view, the decrease of the phase fraction in our elasto-viscoplastic simulation is too large. A smaller decrease could be obtained by increasing the curvature of the homogeneous free energy density around the minima corresponding to the γ and γ' phases. Further work is underway to improve the model on this point.

Finally, improvements of the continuous plasticity model are underway to account for the softening of the matrix behavior as the channel width is increasing. In the present model, a typical channel width was chosen (150 nm) when selecting the values of the viscoplastic parameters of the γ phase. However, during the simulation, there is no coupling between the actual width of a given γ channel and its plastic response. This coupling could be achieved by using a generalized continuum approach, such as a Cosserat continuum [34], or a strain gradient plasticity model (e.g. [35]).

3.5. Conclusion

In the second part of the paper, we have presented a phase field model coupled to a continuum crystal plasticity model. The resulting elasto-viscoplastic phase field model has been applied to study the microstructural evolution of a model AM1 superalloy during creep loading. This model takes into account many important physical phenomena, such as the long-range order in the γ' domains, elastic inhomogeneity, plastic activity, as well as its anisotropy and viscosity. The framework introduced in the present work has allowed a comparison of the respective influence of elastic and plastic driving forces on rafting in Ni-based superalloys. In the considered conditions, we show that plasticity allows raft misalignments with the cubic directions as seen in experiments, and increases the rafting kinetics. Moreover, this elasto-viscoplastic phase field model opens new possibilities for the simulation of microstructural evolutions under mechanical loading when plasticity cannot be neglected.

4. General conclusion

We have shown in this article that the phase field method is a powerful tool for the investigation of microstructures at mesoscale. In the first part of the paper, we analyzed the polytwinned microstructures observed in martensitic alloys, and showed that, due to the large rotations involved in the accommodation mechanism, a correct understanding of the stability of the macrotwin interfaces observed between polytwinned domains requires the use of a geometrically nonlinear modeling. In the second part of the paper, we presented an elasto-viscoplastic phase field model, based on the coupling of the phase field equations to a continuous crystal plasticity model. We discussed the application of this model to the understanding of the microstructural evolutions observed in superalloys under creep and showed that the plastic activity is an essential ingredient in the formation of rafts.

Future developments of the phase field method are of course expected, such as the simultaneous modeling of a displacive transformation and a plastic activity, or the incorporation of a length scale in the viscoplastic equations of the elasto-viscoplastic model.

References

[1] K. Bhattacharya, Microstructure of Martensite: Why it Forms and How it Gives Rise to the Shape-Memory Effect, Oxford University Press, 2003.
[2] Ph. Boullay, D. Schryvers, R.V. Kohn, Bending martensite needles in $Ni_{65}Al_{35}$ investigated by two-dimensional elasticity and high-resolution transmission electron microscopy, Phys. Rev. B 64 (14) (2001).
[3] D. Schryvers, P. Boullay, P.L. Potapov, R.V. Kohn, J.M. Ball, Microstructures and interfaces in Ni–Al martensite: comparing HRTEM observations with continuum theories, Int. J. Solids Struct. 39 (2002) 3543–3554.
[4] D. Schryvers, P. Boullay, R.V. Kohn, J.M. Ball, Lattice deformations at martensite–martensite interfaces in Ni–Al, J. Physique IV 11 (2001) 23–30.
[5] S.S. Antman, Nonlinear Problems of Elasticity, Springer, 2005.
[6] L.D. Landau, E.M. Lifshitz, Theory of Elasticity, Course of Theoretical Physics, Butterworth–Heinemann, 1984.
[7] W.C. Kerr, M.G. Killough, A. Saxena, P.J. Swart, A.R. Bishop, Role of elastic compatibility in martensitic texture evolution, Phase Transitions 69 (3) (1999) 247–270.
[8] A.E. Jacobs, Landau theory of structures in tetragonal-orthorhombic ferroelastics, Phys. Rev. B 61 (10) (2000) 6587–6595.

[9] G.S. Bales, R.J. Gooding, Interfacial dynamics at a first-order phase transition involving strain: Dynamical twin formation, Phys. Rev. Lett. 67 (24) (1991) 3412–3415.
[10] O.U. Salman, Modeling of spatio-temporal dynamics and patterning mechanisms of martensites, PhD thesis, Paris 6, June 2009.
[11] B.K. Muite, O.U. Salman, Computations of geometrically linear and nonlinear Ginzburg–Landau models for martensitic pattern formation, in: P. Šittner, V. Paidar, L. Heller, H. Seiner (Eds.), ESOMAT 2009, EDP Sciences, 2009, p. 03008.
[12] Randall J. LeVeque, Finite Difference Methods for Ordinary and Partial Differential Equations, Steady State and Time Dependent Problems, SIAM, ISBN 978-0-898716-29-0, 2007.
[13] This parameterization is difficult since it requires the knowledge of the twin interfacial energy and elastic constants of the martensite. Unfortunately, as far as we know, these constants are not fully known.
[14] D. Ayrault, A. Fredholm, J.L. Strudel, in: Advanced Materials and Processing Techniques for Structural Applications, Paris, France, Sept. 1987, pp. 71–81.
[15] V. Brien, B. Décamps, Low cycle fatigue of a nickel based superalloys at high temperature: deformation microstructures, Mater. Sci. Eng. 316 (1–2) (2001) 18–31.
[16] N. Matan, D.C. Cox, C.M.F. Rae, R.C. Reed, On the kinetics of rafting in CMSX-4 superalloy single crystals, Acta Mater. 47 (7) (May 1999) 2031–2045.
[17] M. Véron, Y. Bréchet, F. Louchet, Strain induced directional coarsening in Ni based superalloys, Scripta Mater. 34 (1996) 1883.
[18] A. Pineau, Influence of uniaxial stress on the morphology of coherent precipitates during coarsening – elastic energy considerations, Acta Metall. 24 (6) (June 1976) 559–564.
[19] G. Boussinot, Y. Le Bouar, A. Finel, Phase-field simulations with inhomogeneous elasticity: Comparison with an atomic-scale method and application to superalloys, Acta Mater. 58 (2010) 4170–4181.
[20] N. Ratel, G. Bruno, P. Bastie, T. Mori, Plastic strain-induced rafting of γ' precipitates in Ni superalloys: Elasticity analysis, Acta Mater. 54 (19) (2006) 5087–5093.
[21] D. Rodney, A. Finel, Phase field methods and dislocations, in: MRS Symp. Proc., vol. 652, 2001, p. Y4.
[22] Y.U. Wang, Y.M. Jin, A.M. Cuitiño, A.G. Khachaturyan, Nanoscale phase field microelasticity theory of dislocations: model and 3D-simulations, Acta Mater. 49 (2001) 1847–1857.
[23] D. Rodney, Y. Le Bouar, A. Finel, Phase field methods and dislocations, Acta Mater. 51 (1) (2003) 17–30.
[24] R.L.J.M. Ubachs, P.J.G. Schreurs, M.G.D. Geers, Phase field dependent viscoplastic behaviour of solder alloys, Int. J. Solids Struct. 42 (2005) 2533–2558.
[25] T. Uehara, T. Tsujino, N. Ohno, Elasto-plastic simulation of stress evolution during grain growth using a phase field model, J. Cryst. Growth 300 (2007) 530–537.
[26] X.H. Guo, S.Q. Shi, Q.M. Zhang, X.Q. Ma, An elastoplastic phase-field model for the evolution of hydride precipitation in zirconium, part I: smooth specimens, J. Nucl. Mater. 378 (1) (2008) 110–119.
[27] K. Ammar, B. Appolaire, G. Cailletaud, S. Forest, Combining phase field approach and homogenization methods for modelling phase transformation in elastoplastic media, Eur. J. Comput. Mech. 18 (5–6) (2009).
[28] Dominique Jeulin, Samuel Forest (Eds.), Viscoplastic Phase Field Modelling of Rafting in Ni Base Superalloys, Continuum Models and Discrete Systems CMDS, vol. 11, Les Presses de l'École des Mines de Paris, 2008.
[29] G. Boussinot, A. Finel, Y. Le Bouar, Phase-field modeling of bimodal microstructures in nickel-based superalloys, Acta Mater. 57 (3) (2009) 921–931.
[30] G. Cailletaud, Une approche micromécanique phénomènologique du comportement inélastique des métaux, PhD thesis, Ecole Nationale Supérieure des Mines de Paris, 1987.
[31] L. Méric, P. Poubanne, G. Cailletaud, Single crystal modeling for structural calculations: Part 1 – model presentation, J. Eng. Mater. Technol. 113 (1) (1991) 162–170.
[32] A. Gaubert, Y. Le Bouar, A. Finel, Coupling phase field and viscoplasticity to study rafting in Ni-based superalloys, Philos. Mag. 90 (1) (2010) 375–404.
[33] F. Diologent, Comportement en fluage et en traction de superalliages monocristallins à base de Nickel, PhD thesis, Université de Paris 11-Orsay, 2002.
[34] Anais Gaubert, Samuel Forest, Modeling size effect dependence on mechanical behaviour using a Cosserat crystal plasticity framework, in: A. El Azab (Ed.), Tackling Materials Complexities Via Computational Science 3332008 – Multiscale Materials Modeling, Department of Scientific Computing, Tallahassee États-Unis, 2008, pp. 174–177.
[35] E.P. Busso, F.T. Meissonier, N.P. O'Dowd, Gradient-dependant deformation of 2-phase single crystal, J. Mech. Phys. Solids 48 (2000).